Ferroelectricity and multiferroicity in anti–Ruddlesden–Popper structures

Maxime Markov[a], Louis Alaerts[a,b], Henrique Pereira Coutada Miranda[a], Guido Petretto[a], Wei Chen[a], Janine George[a], Eric Bousquet[c], Philippe Ghosez[c], Gian-Marco Rignanese[a], and Geoffroy Hautier[a,b,1]

[a]Institute of Condensed Matter and Nanosciences, Université Catholique de Louvain, B-1348 Louvain-la-Neuve, Belgium; [b]Thayer School of Engineering, Dartmouth College, Hanover, NH 03755; and [c]Theoretical Materials Physics, Quantum Materials Center (Q-MAT), Complex and Entangled Systems from Atoms to Materials (CESAM), Université de Liège, B-4000 Liège, Belgium

Edited by James Rondinelli, Northwestern University, Evanston, IL, and accepted by Editorial Board Member Zachary Fisk March 16, 2021 (received for review December 18, 2020)

Combining ferroelectricity with other properties such as visible light absorption or long-range magnetic order requires the discovery of new families of ferroelectric materials. Here, through the analysis of a high-throughput database of phonon band structures, we identify a structural family of anti–Ruddlesden–Popper phases A_4X_2O (A=Ca, Sr, Ba, Eu, X=Sb, P, As, Bi) showing ferroelectric and antiferroelectric behaviors. The discovered ferroelectrics belong to the new class of hyperferroelectrics that polarize even under open-circuit boundary conditions. The polar distortion involves the movement of O anions against apical A cations and is driven by geometric effects resulting from internal chemical strains. Within this structural family, we show that Eu_4Sb_2O combines coupled ferromagnetic and ferroelectric order at the same atomic site, a very rare occurrence in materials physics.

ferroelectricity | multiferroicity | DFT

Ferroelectric (FE) materials are of great fundamental and applied interest. They are currently used in many technologies such as electric capacitors, piezoelectric sensors and transducers, pyroelectric detectors, nonvolatile memory devices, or energy converters (1–8). For decades, most applications have relied on FE oxide perovskites. However, the need to combine ferroelectricity with other properties such as visible light absorption (9, 10) or long-range magnetic order (11, 12) is driving the search for materials and structural classes beyond perovskites. High-throughput (HT) computational screening is a promising approach to search for materials possessing specific properties. It has been successfully used in a wide variety of fields from thermoelectrics (13, 14) to topological insulators (15–17). Different HT computing approaches have also been used to identify new FEs (18–21). Inspired by these previous studies and using a recently developed large phonon database, we searched for materials exhibiting dynamically unstable polar phonon modes, a signature of potential ferroelectricity. Our HT search identifies a family of (anti)FE materials: the series of anti–Ruddlesden–Popper phases of formula A_4X_2O, where A is a +2 alkali earth or rare-earth element, and X is a −3 anion Bi, Sb, As, and P. We survey how (anti)ferroelectricity subtly depends on the chemistry of A_4X_2O and unveil the physical origin of the polar distortion. Interestingly, the discovered FEs belong to the new class of hyperferroelectrics (22) in which spontaneous polarization is maintained under open-circuit boundary conditions. The anti–Ruddlesden–Popper phases also lead to unique combinations of properties, for instance, a rare combination of ferroelectricity with ferromagnetism in Eu_4Sb_2O.

Results

An HT database of phonon band structures was recently built for more than 2,000 materials present in the Materials Project and mostly originating from the experimental Inorganic Crystal Structure database (23–27). Using this database, we searched for nonpolar structures presenting unstable phonon modes that could lead to a polar structure. This is the signature of a potential FE material (20). We identified Ba_4Sb_2O (space group $I4/mmm$) to be such an FE candidate. Its crystal structure and phonon band structure are shown in Figs. 1*A* and 2*A*, respectively. This phase was reported experimentally by Röhr and George (28), and its crystal structure can be described as analogous to a Ruddlesden–Popper K_2NiF_4 phase, a naturally layered structure alternating rock salt (KF) and perovskite ($KNiF_3$) layers, but for which cation and anions have been switched. Inspired by the terminology used for antiperovskites (29, 30), we will refer to it as an anti–Ruddlesden–Popper phase.

In Ba_4Sb_2O, the large instability of a polar phonon at Γ is compatible with ferroelectricity. Relaxing the structure along this unstable mode confirms the existence of a lower-energy stable phase ($\Delta E = -6.58$ meV per atom) with a noncentrosymmetric space group $I4mm$ and a spontaneous polarization of 9.55 μC/cm^2. The parent $I4/mmm$ structure consists of the periodic repetition of alternative rock salt BaSb and antiperovskite Ba_3SbO layers, along what we will refer to as the z direction. In this structure, O atoms are at the center of regular Ba octahedra (Fig. 1*B*). The polar distortion appearing in the $I4mm$ phase has an overlap of 90% with the unstable polar mode, proving that most of the gain of energy comes from the unstable polar mode. When keeping the center of mass of the system fixed, the related atomic displacement pattern, illustrated in Fig. 1*C*, is dominated by the movement along z of O anion ($\eta_O = 0.212$) against the apical Ba cations, that moves the opposite way

Significance

Ferroelectric materials are of great interest for both applied and fundamental reasons. One of the focuses of the community has been to combine ferroelectricity with other properties such as light absorption or ferromagnetism. Unfortunately, these additional properties have been difficult to add to traditional ferroelectrics such as perovskites, and new families of ferroelectric materials are highly sought. Here, we report on a class of ferroelectric materials offering a geometric mechanism of polar instability and a unique set of properties including the extremely rare combination of ferromagnetic and ferroelectric order.

Author contributions: G.-M.R. and G.H. designed research; M.M., L.A., H.P.C.M., G.P., W.C., and J.G. performed research; M.M., L.A., E.B., P.G., G.-M.R., and G.H. analyzed data; and M.M., E.B., P.G., G.-M.R., and G.H. wrote the paper.

The authors declare no competing interest.

This article is a PNAS Direct Submission. J.R. is a guest editor invited by the Editorial Board.

Published under the PNAS license.

[1]To whom correspondence may be addressed. Email: geoffroy.hautier@dartmouth.edu.

This article contains supporting information online at https://www.pnas.org/lookup/suppl/doi:10.1073/pnas.2026020118/-/DCSupplemental.

Published April 23, 2021.

Downloaded at UNIVERSITE CATHOLIQUE DE LOUVAIN UCL on April 24, 2021

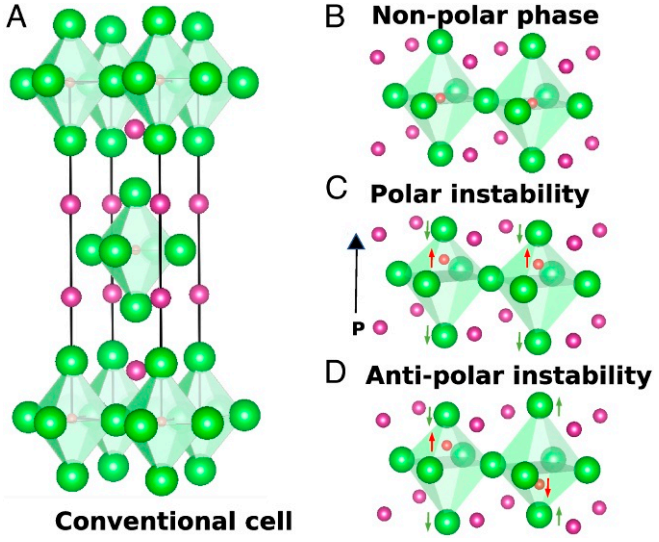


Fig. 1. (*A*) Conventional unit cell representing the anti–Ruddlesden–Popper structure of A_4X_2O. The A cation atoms (in green) form an octahedral cage with an O atom (in red) in its center. The X anion atoms (in violet) act as an environment in the voids surrounding the cages. Adopting a schematic representation with two neighboring octahedra surrounded by X atoms, we label three potentially metastable phases. (*B*) In the reference nonpolar phase, the two O atoms are located in the middle of the octahedral cages of A cations (shaded green), being equidistant from the two apical A cations. (*C*) Upon the polar distortion, the O atoms move upward in the direction of apical A cations moving downward, as indicated by the red and green arrows, respectively. This results in a loss of centrosymmetry and, thus, leads to a finite polarization value along this direction. (*D*) In the case of an antipolar distortion, the O and A cation atoms in neighboring cages move in opposite directions, canceling out the polarization. In the plots, the displacements of the atoms have been amplified compared to their actual values (*Results*) in order to make them easily understood.

($\eta_O = -0.029$).* This cooperative movement of Ba and O atoms is responsible for the spontaneous polarization along z, while Sb and the other Ba atoms play a more negligible role (in reducing the polarization by only 4%). Contrary to regular Ruddlesden–Popper compounds, that can show in-plane ferroelectricity but are not unfavorable to out-of-plane polarization, the polarization here is along the stacking direction. Also, Ba_4Sb_2O does not show the antiferrodistortive instabilities ubiquitous in traditional Ruddlesden–Popper phases (31–34).

Next to Ba_4Sb_2O, other alkali earth atoms such as Ca and Sr have been reported to form in the same structure (35, 36). To further explore the role of chemistry on ferroelectricity, we plot, in Fig. 2, the phonon band structure of the A_4Sb_2O series, with A=Ca, Sr, and Ba, in their $I4/mmm$ phase. All compounds are insulating. We observe that the polar instability is reduced in Sr_4Sb_2O in comparison to Ba_4Sb_2O and is totally suppressed in Ca_4Sb_2O.

However, the existence of a polar instability is not enough to guarantee an FE ground state. Other competing phases (e.g., antipolar distortions) could be more stable than the polar phase (37). Indeed, the presence of phonon instabilities at points other than Γ (e.g., X or L) indicates the possibility of such competing phases (Fig. 2). By following the eigendisplacements of individual and combined unstable modes, we confirm that the lowest-energy phase is polar for Ba_4Sb_2O. Combined with its insulating character [Heyd–Scuseria–Ernzerhof (HSE) direct band gap is 1.22 eV] and the moderate energy difference between nonpolar and polar states, this confirms an FE ground state. In Sr_4Sb_2O, we find that the ground state is instead an antipolar $C2/m$ phase, as illustrated in Fig. 1*D* (see *SI Appendix*, Fig. S2 for the entire crystal structure of the antipolar distortion of Sr_4Sb_2O). This antipolar phase is only $\Delta E = 0.57$ meV per atom lower in energy than the polar phase. Hence, the polar phase could be stabilized under moderate electric fields, making Sr_4Sb_2O a potential antiferroelectric compound (38). Using $E_c \approx \Delta E/\Omega_0 P_s$, we estimate the critical field E_c in Sr_4Sb_2O to be 81 kV/cm, which could be easily accessible in experiment. Turning to the atomic pattern of antipolar distortion, we see that it corresponds to a simple modulation of the polar distortion, with O atoms in neighboring octahedra moving in opposite directions and canceling out the macroscopic polarization (Fig. 1*D*). As such, Sr_4Sb_2O would therefore appear as a rare example of Kittel-type antiferroelectric (38–40).

We also note an intriguing discontinuity at Γ in the unstable phonon branch of Ba_4Sb_2O (Fig. 2). We rationalize this discontinuity by noting that the unstable optical mode is polarized along the z axis, so that it is transverse (TO) along Γ–X and Γ–Y and longitudinal (LO) along Γ–Z. This is further illustrated in Fig. 2 by the gray smearing on top of the phonon dispersion curves that indicates the longitudinal character $L_{\mathbf{q},\nu}$. The latter was defined as $L_{\mathbf{q},\nu} = \mathbf{q} \cdot (Z^*_\alpha \cdot \Delta_{\alpha,\nu})/|Z^*_\alpha \cdot \Delta_{\alpha,\nu}|$, where $\mathbf{q}$ is the phonon wavevector, Z^* is the Born effective charge matrix, and Δ is the eigendisplacement of atom α with phonon mode index ν. Interestingly, we notice that the overlap between the lowest LO and TO mode eigendisplacements is 90% and that the LO–TO splitting is rather small, so that the LO mode remains strongly unstable. Such a feature was previously reported in $LiNbO_3$ (41), or in hexagonal ABC FEs, and is the fingerprint of so-called hyperferroelectricity (22). This demonstrates that Ba_4Sb_2O is not only FE but belongs to the interesting subclass of hyperferroelectrics in which a spontaneous polarization is maintained even under open-circuit boundary conditions (electrical boundary conditions with the electric displacement field $D = 0$), so even when the unscreened depolarizing field tries to cancel out the bulk polarization.

The chemical versatility of the anti–Ruddlesden–Popper phases is high. Beyond A_4Sb_2O oxo-antimonides, synthesis of oxo-phosphides, oxo-arsenates, and oxo-bismuthides have been reported (see *SI Appendix*). We have systematically computationally explored the entire range of A_4X_2O structures (A=Ca, Sr, Ba; X=Sb, P, As, Bi). The phonon band structures are all plotted in *SI Appendix*, Fig. S1, and the results of the relaxation along all unstable phonon modes are presented in Table 1. More information on the phases competing for each chemistry is available in *SI Appendix*. We found that all Ca-based compounds are paraelectric. Only Ba_4As_2O and Ba_4Sb_2O show a polar ground state; the ground states are antipolar most of the time. We note that we only found a few instabilities through octahedra rotations and tilts in the anti–Ruddlesden–Popper phase, while they are common in standard Ruddlesden–Popper structures such as $(Ca,Sr)_3Ti_2O_7$ (42), $Ca_3Zr_2S_7$ (43), and $La_2SrCr_2O_7$ (44). One of the appeals of perovskites is their strong chemical tunability, as many different chemical substitutions can be performed tuning the FE properties (34, 37). It appears that similar tunability could be available for A_4X_2O. Moreover, as our described anti–Ruddlesden–Popper structure corresponds to $n = 1$ in the traditional series $A_{3n+1}X_{n+1}O_{n+1}$, one could consider tuning properties by varying n to higher values, possibly by thin-film growth (45, 46).

We now turn to the origin of the polar distortion in A_4X_2O. We especially focus on the A_4Sb_2O series which shows a transition in the nature of the ground state from strongly polar for Ba to antipolar for Sr and nonpolar for Ca. The anti–Ruddlesden–Popper structure shows a polar displacement of an anion in an octahedral cationic cage, and it is natural to make the analogy

*In the *I*4*mm* ground state, the motion of the top apical O atom has been reduced by anharmonic couplings with other modes.

Downloaded at UNIVERSITE CATHOLIQUE DE LOUVAIN UCL on April 24, 2021

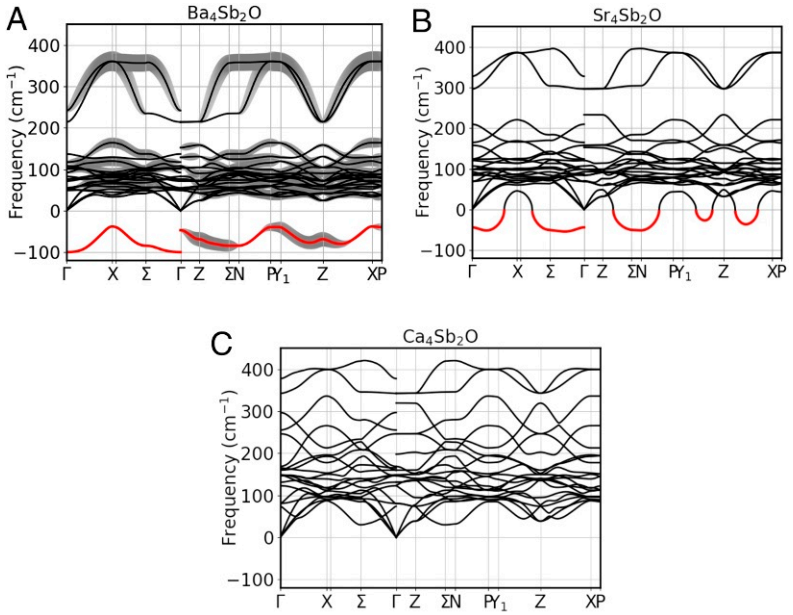


Fig. 2. Phonon dispersion curves of $I4/mmm$ A_4Sb_2O parent structures, with the A cation atoms being (*A*) Ba, (*B*) Sr, and (*C*) Ca. Unstable phonon modes are highlighted in red. Change of the cation atom from the heavy Ba atom to the lighter Ca atom leads to the stabilization of the paralectric parent structure. On top of the phonon dispersion of Ba_4Sb_2O, we plot the longitudinal character $L_{(\mathbf{q},\nu)}$ to distinguish between LO and TO modes and highlight a discontinuity at Γ.

PHYSICS

with traditional FE perovskites such as $BaTiO_3$, where a cation moves in an anionic octahedral cage. However, the analysis of the Born effective charges hints at a very different physical mechanism in both situations. While FE oxide perovksites can show anomalously high Born effective charges (Z^*_{Ti} = +7.25 e, Z^*_0 = −5.71 e) (47), the Born effective charges in Ba_4Sb_2O are closer to the nominal charges (Z^*_{Ba} = +2.67 e, Z^*_0 = −2.71 e). This indicates a more ionic bonding between the O and alkali earth atoms and that dynamical charge transfer is not as important as in oxide perovskites (48). This conclusion is further confirmed by the crystal orbital Hamilton population (COHP) analysis (49–51) showing rather weak covalent character of Ba–O bonds in Ba_4Sb_2O in contrast to the much stronger covalent character of Ti–O bonds in $BaTiO_3$, with integrated COHP energy being one order of magnitude higher than the one in Ba_4Sb_2O. In passing, we note that, while Born effective charges are lower in anti–Ruddlesden–Popper structures, their large atomic displacements (e.g., 0.40 Å for O and −0.20 Å for one of Ba atoms in Ba_4Sb_2O) maintain a reasonable polarization. This analysis points to an FE distortion driven by a geometrical effect with the simple picture of an O atom relatively free to move in a too large cationic cage. To further confirm this picture, we study the interatomic force constants (IFCs) in real space. We observe that the on-site IFC of the O atom, quantifying the restoring force that it feels when displaced with respect to the rest of the crystal, is close to zero in Ba_4X_2O along the z (out-of-plane) direction, and one order of magnitude smaller than in-plane. This highlights that the O atoms are almost free to move along z in the $I4/mmm$ phase.

The close to nominal Born effective charges and very low on-site IFC are both characteristics of geometrically driven ferroelectricity as described in fluoride perovskites (52). The geometric nature of the instability naturally explains why going from Ba to Sr and Ca weakens the polar instability. Indeed, the on-site IFCs of the O atom along z increase as we go from Ba to Ca (0.17, 0.99, and 1.79 eV/Å^2) and as the cation to O distance along z progressively decreases (d_{AO}= 3.08, 2.88, and 2.66 Å). The smaller room for the O movement lowers the polar instability for Sr compared to Ba and cancels it for Ca. The local character of the structural instability in real space is confirmed by its fully delocalized character in reciprocal space in Fig. 2. The local and geometric nature of the structural instability is also consistent with the hyperferroelectric character (53) and the possible emergence of antiferroelectricity.

In A_4X_2O anti–Ruddlesden–Popper compounds, the O atoms are surrounded by an octahedron of A atoms, showing a local environment similar to that experienced in the AO rock salt phases. The latter are constituted by regular octahedron units and are paraelectric. However, it has been predicted theoretically (54) and recently confirmed experimentally (55) that rock

Table 1. Classification of the A_4X_2O family according to their electric state

	Bi	Sb	As	P
Ba	Anti-FE *C*2/*m*, −7.37 $\frac{\text{meV}}{\text{atom}}$	FE *I*4*mm*, −6.58 $\frac{\text{meV}}{\text{atom}}$	FE *I*4*mm*, −5.93 $\frac{\text{meV}}{\text{atom}}$	Anti-FE *Cmce*, −21.24 $\frac{\text{meV}}{\text{atom}}$
Sr	Anti-FE *C*2/*m*, −1.74 $\frac{\text{meV}}{\text{atom}}$	Anti-FE *C*2/*m*, −0.83 $\frac{\text{meV}}{\text{atom}}$	Paraelectric *C*2/*m*, −0.65 $\frac{\text{meV}}{\text{atom}}$	Anti-FE *Cmce*, −2.87 $\frac{\text{meV}}{\text{atom}}$
Ca	Paraelectric *I*4/*mmm*, 0.0 $\frac{\text{meV}}{\text{atom}}$	Paraelectric *I*4/*mmm*, 0.0 $\frac{\text{meV}}{\text{atom}}$	Paraelectric *I*4/*mmm*, 0.0 $\frac{\text{meV}}{\text{atom}}$	Paraelectric *I*4/*mmm*, 0.0 $\frac{\text{meV}}{\text{atom}}$

Paraelectric refers to a stable structure or a structure with nonpolar transition only, FE is a material with the nonpolar to polar transition, anti-FE is a material with nonpolar to nonpolar transition with a polar phase being slightly higher in energy with respect to the lowest phase. The energy difference between the parent and the lowest child phase as well as the space group of the ground phase are shown. The parent phase has a space group *I*4/*mmm*; the polar and antipolar phase space groups are *I*4*mm* and *C*2/*m*, respectively. For A_4P_2O, another orthorhombic antipolar phase emerges.

Downloaded at UNIVERSITE CATHOLIQUE DE LOUVAIN UCL on April 24, 2021

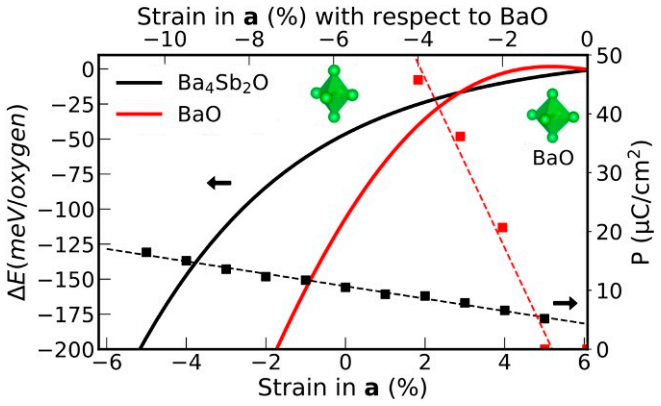


Fig. 3. Energy difference between child and parent phases (solid lines) and polarization (dashed lines) of Ba_4Sb_2O (black curves) and BaO (red curves) as a function of in-plane strain computed with PBE functional. The data were fitted with linear function and the fourth-order polynomials for polarization and energy difference respectively. Regular BaO and strained elongated Ba_4Sb_2O octahedra are shown.

salt alkali earth can become FE beyond a critical compressive epitaxial strain. Fig. 3 shows the energy difference and polarization between the paraelectric and FE phases as a function of the compressive strain for BaO (red) and Ba_4Sb_2O (black). The FE phase becomes favored for BaO above a compressive strain of 1%. On the other hand, the unstrained Ba_4X_2O has Ba_6O octahedra distorted to the equivalent of around −6% in BaO. Applying a tensile strain on Ba_4X_2O moves the octahedral geometry toward unstrained rock salt BaO and lowers the polar instability. Additionally, the c/a ratio describing the octahedron elongation is ∼1.2 and close to that of the FE phase of BaO at that strain. This highlights that, in Ba_4X_2O, the surrounding atoms impose an internal, chemical strain on the Ba_6O cages. This natural strain induces ferroelectricity, as previously highlighted in strained BaO. We note that such a level of strain (6%) is difficult to reach within epitaxial films of rock salt (55). In Ba_4Sb_2O, however, polarization increases much more slowly with strain than in BaO, due to the presence of Sb atoms which limit the deformation of octahedra in the FE phase (see *SI Appendix*). While we focused on the X=Sb antimonide series here, the trend with Ba >Sr > Ca in terms of polar distortion is present across all chemistries from X=P, As, Bi, and Sb (see *SI Appendix*).

Compared to common perovskite-related structures, the A_4X_2O family offers opportunities for achieving properties that have been traditionally difficult to combine with traditional FE perovskites. Anti–Ruddlesden–Popper materials show typically smaller band gaps compared to oxide perovskites. While tetragonal $P4mm$ $BaTiO_3$ shows an indirect optical band gap of about 3.2 eV [1.67 eV in generalized gradient approximations (GGA) between O 2p and Ti 3d states], we estimated the band gap of Ba_4Sb_2O to be 1.22 eV, using the HSE hybrid functional [0.67 eV in Perdew–Burke–Ernzerhof (PBE)]. The band structure of Ba_4Sb_2O is shown in Fig. 4, highlighting a direct gap at Z between Ba 5d (conduction bands) and Sb 3p states (valence bands). Other A_4X_2O compounds show similar band gaps in the range from 0.57 eV to 1.00 eV in PBE (see *SI Appendix*, Fig. S4). Such FEs with small band gaps compatible with visible light could be very useful in the field of ferroelectricity-driven photovoltaics (9, 10, 56–59).

Another grand challenge has been to combine ferroelectricity with magnetic long-range order in magnetoelectric multiferroics. The traditional mechanism of polar instability in the B site of a perovskite has been deemed difficult to combine with ferroelectricity, since the nonmagnetic d^0 character of the B site transition metal is often necessary to favor ferroelectricity (60, 61). Combining polar distortion on one site and magnetism on another site such as in $EuTiO_3$ or $BiFeO_3$ (11, 62) or moving toward improper ferroelectricity as in $YMnO_3$ has led to magnetoelectric multiferroics (63–65). The geometrically driven polar instability demonstrated in anti–Ruddlesden–Popper structure offers an alternative opportunity for multiferroicity. Magnetic +2 rare-earth atoms often substitute to alkali earth, and Eu_4Sb_2O has been experimentally reported to form in the anti–Ruddlesden–Popper structure (66). Computing phonon band structures and relaxing the structure along the unstable modes, we found that Eu_4Sb_2O is FE. Similar to Ba_4Sb_2O, the geometric polar instability in Eu_4Sb_2O involves, directly, the movement of nonmagnetic O against the magnetic apical Eu^{2+}. This is likely to couple magnetism and ferroelectricity. Our calculations show that Eu_4Sb_2O exhibits a ferromagnetic ground ($E_{FM} - E_{AFM} = 1.6$ meV) state with an easy axis pointing along the c direction and along the polarization (E_{MAE}= 19 μeV). We estimate the magnetic Curie temperature to be ∼24 K (see *Methods*). Most magnetoelectric multiferroic materials, including the most studied $BiFeO_3$, are antiferromagnetic. Despite their technological importance, there are very few examples of materials combining ferromagnetic and FE order (67), and the few known ones are double perovskites [e.g., Pb_2CoWO_6 (68) or the R_2NiMnO_6/La_2NiMnO_6 heterostructures (69)] where magnetism and ferroelectricity come from different sites. Eu_4Sb_2O, similar to its parent rock salt EuO, is a ferromagnetic insulating oxide (70). The coexistence of ferromagnetism and ferroelectricity has just been confirmed experimentally in epitaxially strained EuO films (55) and is naturally appearing in Eu_4Sb_2O anti–Ruddlesden–Popper phase. The magnetic space group $I4m'm'$ is compatible with linear magnetoelectric coupling, and the magnetoelectric tensor has the following form (71):

$$\alpha_{ME} = \begin{pmatrix} \alpha_{xx} & 0 & 0 \\ 0 & \alpha_{xx} & 0 \\ 0 & 0 & \alpha_{zz} \end{pmatrix}. \quad [1]$$

More quantitatively, the computation of the linear magnetoelectric tensor in Eu_4Sb_2O confirms that a coupling is present with a small but nonzero value: $\alpha_{xx} = 0.10$ ps/m (ionic contribution 0.08 ps/m and 0.02 electronic contribution), $\alpha_{zz} = 0.02$ ps/m (ionic contribution 0.01 ps/m and 0.01 electronic contribution). We note that other rare-earth–based anti–Ruddlesden–Popper

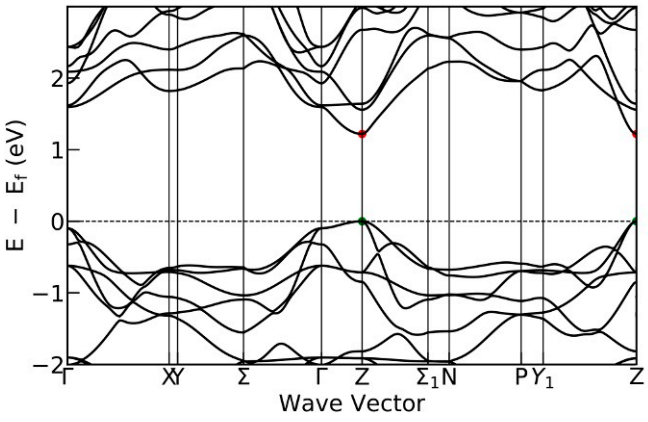


Fig. 4. Electronic band structure of Ba_4Sb_2O in its *I4mm* polar phase along the high-symmetry directions with PBE functional with a scissors correction of 0.55 eV. The direct band gap at Z point (1.22 eV) is marked by red and green points for the conduction and valence bands.

Downloaded at UNIVERSITE CATHOLIQUE DE LOUVAIN UCL on April 24, 2021

phases are known to exist: Eu_4As_2O (72), Eu_4Bi_2O (73), Yb_4As_2O (74), Yb_4Sb_2O (75), and Sm_4Bi_2O (76). It is possible that, in addition to Eu_4Sb_2O, other anti–Ruddlesden–Popper compounds are magnetoelectric multiferroics.

Conclusions

Following a data-driven approach based on an HT search within a database of phonons, we have identified a family of A_4X_2O (A=Ba, Sr, Ca, Eu and X=Bi, Sb, As, P) materials forming in an anti–Ruddlesden–Popper structure and showing (anti)FE properties. The discovered mechanism of polar distortion involves the movement of an anion in a cation octahedron. This distortion is geometrically driven and controlled by the natural strain present in the cation octahedron. This mechanism leads to hyperferroelectricity but also offers the possibility of combining ferroelectricity with properties uncommon in traditional perovskite-based structures such as small band gaps or magnetism. More specifically, we show that Eu_4Sb_2O exhibits a rare combination of ferromagnetic and FE order coupled through linear magnetoelectric coupling. The wide range of chemistries forming in the anti–Ruddlesden–Popper structure offers a tunability similar to that of perovskite structures in terms of strain, chemistry, and heterostructures and opens an avenue for FEs research.

Methods

The HT search for novel FEs was performed using a recently published phonon database (23). We first selected the unstable materials presenting at least one phonon mode m with imaginary frequencies $\omega_m(\mathbf{q})$ within a **q**-point region of the Brillouin zone. For each of these materials and modes, we focused on the high-symmetry **q** points commensurate with a $2\times2\times2$ supercell. We generated a set of new structures by moving the atoms in that supercell according to the displacements corresponding to the different modes and **q** points. The symmetry of each new structure was analyzed using the spglib library (77) with a tolerance of 10^{-6} Å and 1° on angles. Then, the new structures were categorized as polar or nonpolar, depending on their point group. Finally, after relaxing all of the structures in the set, we classified the materials as paraelectric (when all of the structures in the set are nonpolar and the polarization is thus always zero), FE (when the ground state is polar, hence possessing a finite polarization value), or anti-FE (when the ground state is nonpolar but there exists at least one polar phase in the set slightly higher in energy). In the latter case, the material can be driven to the polar phase upon application of a strong enough electric field and thus acquire the nonzero polarization.

Density functional theory (DFT) calculations were performed with the ABINIT (78) and Vienna Ab initio Simulation Package (VASP) (79, 80) codes. PBEsol exchange–correlation was used everywhere, if not otherwise noted. PseudoDojo norm-conserving scalar-relativistic pseudopotentials (ONCVSP v0.3) (81, 82) were used in ABINIT. The Brillouin zone was sampled using a density of approximately 1,500 points per reciprocal atom. All of the structures were relaxed with strict convergence criteria, that is, until all of the forces on the atoms were below 10^{-6} Ha/Bohr, and the stresses were below 10^{-4} Ha/Bohr^3 (23). The phonon band structures were computed within the density functional perturbation theory (DFPT) formalism as implemented in ABINIT (83, 84) using a **q**-point sampling density similar to the **k** point one, although for Γ-centered grids. The polarization was computed with both the Berry-phase and Born effective charge approaches. GGA_PBE projector-augmented wave (PAW) pseudopotentials were used in VASP (85). The structures were relaxed up to 10^{-3} eV/Å. The cutoff energy was set to 520 eV, and electronic convergence was done up to 10^{-7} eV. The **k**-point sampling was similar to the one used in ABINIT. Both codes yield essentially the same results in the identification of the ground state phase. The use of PBE exchange–correlation potential does not change the ground state phase as well. The Lobster calculations were performed based on VASP DFT calculations. (49–51, 86) We used the following basis functions from the pbeVaspFit2015 for the projections: Ca (3p, 3s, 4s), Sr (4p, 4s, 5s), Ba (5s, 5p, 6s), Sb (5p, 5s), O (2p, 2s), and Ti (3d, 3p, 4s). The **k**-point grids for these calculations were at least $12\times12\times3$ for A_4X_2O and $13\times13\times13$ for $BaTiO_3$. The magnetic structure calculations for Eu_4Sb_2O were performed with VASP code. The Eu pseudopotential includes 17 electrons in the valence. For the DFT+U calculations, the parameters were set to U = 6.0 eV and J = 0.0 eV to accurately describe the localized Eu f orbitals. Good electronic convergence up to 10^{-8} eV was obtained with an energy cutoff 600 eV and $6\times6\times3$ **k**-point grid. The results were double-checked with a $12\times12\times6$ **k**-point grid. The Curie temperature was estimated using the random-phase approximation (70, 87). The phonon band structure for Eu_4Sb_2O was computed through the finite displacements method as implemented in Phonopy (77) using a $2\times2\times2$ supercell. The electronic and ionic parts of magnetoelectric tensor were computed with the magnetic field (88) and finite displacements (89) approaches, respectively. Spin–orbit coupling was included in the calculations of magnetocrystalline anisotropy and magnetoelectric coupling. Magnetic symmetries and the form of magnetoelectric tensor were identified via the Bilbao crystallographic server.

Data Availability. All study data are included in the article and *SI Appendix*.

ACKNOWLEDGMENTS. This work was funded by the US Department of Energy, Office of Science, Office of Basic Energy Sciences, Materials Sciences and Engineering Division under Contract DE-AC02-05-CH11231: Materials Project Program KC23MP. H.P.C.M. acknowledges financial support from Le Fonds de la Recherche Scientifique (FRS-FNRS) through Projet de Recherche (PDR) Grants HTBaSE (T.1071.15). J.G. acknowledges funding from the European Union's Horizon 2020 research and innovation program under the Marie Skłodowska-Curie Grant Agreement 837910. We thank the Consortium des Équipements de Calcul Intensif en Fédération Wallonie Bruxelles for computational resources. Additionally, the present research benefited from computational resources made available on the Tier-1 supercomputer of the Fédération Wallonie-Bruxelles, infrastructure funded by the Walloon Region under Grant Agreement 1117545.

1. M. E. Lines, A. M. Glass, *Principles and Applications of Ferroelectrics and Related Materials* (Clarendon, ed. 1, 1977).
2. J. F. Scott, C. A. Paz de Araujo, Ferroelectric memories. *Science* **246**, 1400–1405 (1989).
3. J. F. Scott, Applications of modern ferroelectrics. *Science* **315**, 954–959 (2007).
4. V. Garcia *et al.*, Giant tunnel electroresistance for non-destructive readout of ferroelectric states. *Nature* **460**, 81–84 (2009).
5. C. R. Bowen, H. A. Kim, P. M. Weaver, S. Dunn, Piezoelectric and ferroelectric materials and structures for energy harvesting applications. *Energy Environ. Sci.* **7**, 25–44 (2014).
6. L. W. Martin, A. M. Rappe, Thin-film ferroelectric materials and their applications. *Nat. Rev. Mater.* **2**, 16087 (2017).
7. T. Y. Kim, S. K. Kim, S.-W. Kim, Application of ferroelectric materials for improving output power of energy harvesters. *Nano Converg.* **5**, **30** (2018).
8. A. Chanthbouala *et al.*, A ferroelectric memristor. *Nat. Mater.* **11**, 860–864 (2012).
9. H. Huang, Ferroelectric photovoltaics. *Nat. Photonics* **4**, 134–135 (2010).
10. Y. Li, D. J. Singh, Properties of the ferroelectric visible light absorbing semiconductors: $Sn_2P_2Se_6$ and $Sn_2P_2Se_6$. *Phys. Rev. Mater.* **1**, 075402 (2017).
11. N. A. Spaldin, R. Ramesh, Advances in magnetoelectric multiferroics. *Nat. Mater.* **18**, 203–212 (2019).
12. N. A. Spaldin, Multiferroics beyond electric-field control of magnetism. *Proc. R. Soc. A* **476**, 20190542 (2020).
13. W. Chen *et al.*, Understanding thermoelectric properties from high-throughput calculations: Trends, insights, and comparisons with experiment. *J. Mater. Chem. C* **4**, 4414–4426 (2016).
14. F. Ricci *et al.*, An *ab initio* electronic transport database for inorganic materials. *Sci. Data* **4**, 170085 (2017).
15. X. Li, Z. Zhang, Y. Yao, H. Zhang, High throughput screening for two-dimensional topological insulators. *2D Mater.* **5**, 045023 (2018).
16. Z. Zhang *et al.*, High-throughput screening and automated processing toward novel topological insulators. *J. Phys. Chem. Lett.* **9**, 6224–6231 (2018).
17. K. Choudhary, K. F. Garrity, F. Tavazza, High-throughput discovery of topologically non-trivial materials using spin-orbit spillage. *Sci. Rep.* **9**, 8534 (2019).
18. E. Kroumova, M. I. Aroyo, J. M. Perez-Mato, Prediction of new displacive ferroelectrics through systematic pseudosymmetry search. Results for materials with *Pba*2 and *Pmc2*$_1$ symmetry. *Acta Crystallogr. B* **58**, 921–933 (2002).
19. J. W. Bennett, K. F. Garrity, K. M. Rabe, D. Vanderbilt, Hexagonal *abc* semiconductors as ferroelectrics. *Phys. Rev. Lett.* **109**, 167602 (2012).
20. K. F. Garrity, High-throughput first-principles search for new ferroelectrics. *Phys. Rev. B* **97**, 024115 (2018).
21. T. E. Smidt, S. A. Mack, S. E. Reyes-Lillo, A. Jain, J. B. Neaton, An automatically curated first-principles database of ferroelectrics. *Sci. Data* **7**, 72 (2020).
22. K. F. Garrity, K. M. Rabe, D. V. Hyperferroelectrics, Proper ferroelectrics with persistent polarization. *Phys. Rev. Lett.* **112**, 127601 (2014).
23. G. Petretto *et al.*, High-throughput density-functional perturbation theory phonons for inorganic materials. *Sci. Data* **5**, 180065 (2018).
24. G. Petretto, X. Gonze, G. Hautier, G.-M. Rignanese, Convergence and pitfalls of density functional perturbation theory phonons calculations from a high-throughput perspective. *Comput. Mater. Sci.* **144**, 331–337 (2018).
25. A. Jain *et al.*, The Materials Project: A materials genome approach to accelerating materials innovation. *APL Mater.* **1**, 011002 (2013).
26. F. H. Allen, G. Bergerhoff, R. Sievers, *Crystallographic Databases* (International Union of Crystallography, Chester, United Kingdom, 1987).

Downloaded at UNIVERSITE CATHOLIQUE DE LOUVAIN UCL on April 24, 2021

27. D. Zagorac, H. Müller, S. Ruehl, J. Zagorac, S. Rehme, Recent developments in the inorganic crystal structure database: Theoretical crystal structure data and related features. *J. Appl. Crystallogr.* **52**, 918–925 (2019).
28. C. Röhr, R. George, Crystal structure of barium antimonide oxide, Ba_4Sb_2O. *Z. Kristallogr.* **211**, 478 (1996).
29. S. V. Krivovichev, Minerals with antiperovskite structure: A review. *Z. Kristallogr.* **223**, 109–113 (2008).
30. M. Bilal, S. Jalali-Asadabadi, R. Ahmad, I. Ahmad, Electronic properties of antiperovskite materials from state-of-the-art density functional theory. *J. Chem.* **2015**, 495131 (2015).
31. D. A. Freedman, T. A. Arias, Impact of octahedral rotations on Ruddlesden-Popper phases of antiferrodistortive perovskites. arXiv [Preprint] (2009). https://arxiv.org/abs/0901.0157. Accessed 18 December 2020.
32. T. Xu, T. Shimada, J. Wang, T. I. Kamura, Antiferroelectric and antiferrodistortive phase transitions in Ruddlesden-Popper Pb_2TiO_4 from first-principles. *Coupl. Syst. Mech.* **6**, 29–40 (2017).
33. Y. Zhang, M. P. K. Sahoo, T. Shimada, T. Kitamura, J. Wang, Strain-induced improper ferroelectricity in Ruddlesden-Popper perovskite halides. *Phys. Rev. B* **96**, 144110 (2017).
34. Y. Zhang, J. Wang, P. Ghosez, Unraveling the suppression of oxygen octahedra rotations in $A_3B_2O_7$ Ruddlesden-Popper compounds: Engineering multiferroicity and beyond. *Phys. Rev. Lett.* **125**, 157601 (2020).
35. C. Hadenfeldt, H.U. Terschüren, Darstellung und Kristallstruktur der Strontium und Bariumpnictidoxide Sr_4P_2O, Sr_4As_2O, Ba_4P_2O und Ba_4As_2O. *Z. Anorg. Allg. Chem.* **597**, 69–78 (1991).
36. H. Limartha, B. Eisenmann, H. Schäfer, H. A. Graf, Preparation and crystal structure of Ca_4Sb_2O. *Z. Naturforsch. B Chem. Sci.* **35**, 1518–1524 (1980).
37. N. A. Benedek, J. M. Rondinelli, H. Djani, P. Ghosez, P. Lightfoot, Understanding ferroelectricity in layered perovskites: New ideas and insights from theory and experiments. *Dalton Trans.* **44**, 10543–10558 (2015).
38. Karin. M. Rabe, "Antiferroelectricity in oxides: A reexamination" , in *Functional Metal Oxides: New Science and Novel Applications*, S. B. Ogale, T. V. Venkatsan, M. G. Blamire, Eds. (John Wiley, 2013), pp. 221–244.
39. C. Kittel, Theory of antiferroelectric crystals. *Phys. Rev.* **82**, 729 (1951).
40. C. Milesi-Brault *et al.*, Archetypal soft-mode-driven antipolar transition in francisite $Cu_3Bi(SeO_3)_2O_2Cl$. *Phys. Rev. Lett.* **124**, 097603 (2020).
41. M. Veithen, P. Ghosez, First-principles study of the dielectric and dynamical properties of lithium niobate. *Phys. Rev. B* **65**, 214302 (2002).
42. R. Zhang, M. S. Senn, M. A. Hayward, Directed lifting of inversion symmetry in Ruddlesden–Popper oxide–fluorides: Toward ferroelectric and multiferroic behavior. *Chem. Mater.* **28**, 8399–8406 (2016).
43. Y. Zhang, T. Shimada, T. Kitamura, J. Wang, Ferroelectricity in Ruddlesden–Popper chalcogenide perovskites for photovoltaic application: The role of tolerance factor. *J. Phys. Chem. Lett.* **8**, 5834–5839 (2017).
44. R. Zhang *et al.*, $La_2SrCr_2O_7$: Controlling the tilting distortions of $n = 2$ Ruddlesden–Popper phases through a-site cation order. *Inorg. Chem.* **55**, 8951–8960 (2016).
45. I. B. Sharma, D. Singh, Solid state chemistry of Ruddlesden-Popper type complex oxides. *Bull. Mater. Sci.* **21**, 363–374 (1998).
46. Y. F. Nie *et al.*, Atomically precise interfaces from non-stoichiometric deposition. *Nat. Commun.* **5**, 4530 (2014).
47. Ph. Ghosez, J.-P. Michenaud, X. Gonze, Dynamical atomic charges: The case of ABO_3 compounds. *Phys. Rev. B* **58**, 6224–6240 (1998).
48. P. Ghosez, X. Gonze, J. P. Michenaud, Coulomb interaction and ferroelectric instability of $BaTiO_3$. *Europhys. Lett.* **33**, 713–718 (1996).
49. R. Dronskowski, P. E. Bloechl, Crystal orbital Hamilton populations (COHP): Energy-resolved visualization of chemical bonding in solids based on density-functional calculations. *J. Phys. Chem.* **A97**, 8617–8624 (1993).
50. S. Maintz, V. L. Deringer, A. L. Tchougreeff, R. Dronskowski, LOBSTER: A tool to extract chemical bonding from plane-wave based DFT. *J. Comput. Chem.* **37**, 1030–1035 (2016).
51. R. Nelson *et al.*, LOBSTER: Local orbital projections, atomic charges, and chemical-bonding analysis from projector-augmented-wave-based density-functional-theory. *J. Comput. Chem.* **41**, 1931–1940 (2020).
52. A. C. Garcia-Castro, N. A. Spaldin, A. H. Romero, E. Bousquet, Geometric ferroelectricity in fluoroperovskites. *Phys. Rev. B* **89**, 104107 (2014).
53. M. Khedidji, D. Amoroso, H. Djani, Microscopic mechanisms behind hyperferroelectricity. *Phys. Rev. B* **103**, 014116 (2021).
54. E. Bousquet, N. A. Spaldin, P. Ghosez, Strain-induced ferroelectricity in simple rocksalt binary oxides. *Phys. Rev. Lett.* **104**, 037601 (2010).
55. V. Goian *et al.*, Making EuO multiferroic by epitaxial strain engineering. *Commun. Mater.* **1**, 74 (2020).
56. S. M. Young, Z. Fan, A. M. Rappe, First-principles calculation of the bulk photovoltaic effect in bismuth ferrite. *Phys. Rev. Lett.* **109**, 236601 (2012).
57. Y. Peng, S. Chiou, C. Hsiao, C. Ouyang, C.-H. Tu, Remarkably enhanced photovoltaic effects and first-principles calculations in neodymium doped $BiFeO_3$. *Sci. Rep.* **4**, 45164 (2017).
58. I. Grinberg *et al.*, Perovskite oxides for visible-light-absorbing ferroelectric and photovoltaic materials. *Nature* **503**, 509–512 (2013).
59. J. He, C. Franchini, J. M. Rondinelli, Lithium niobate-type oxides as visible light photovoltaic materials. *Chem. Mater.* **28**, 25–29 (2016).
60. N. A. Hill, Why are there so few magnetic ferroelectrics? *J. Phys. Chem. B* **104**, 6694–6709 (2000).
61. N. A. Spaldin, "Analogies and differences between ferroelectrics and ferromagnets" in *Physics of Ferroelectrics*, K. M. Rabe, C. H. Ahn, J.-M. Triscone, Eds., (Springer-Verlag, 2007), pp. 175–218.
62. V. V. Shvartsman, P. Borisov, W. Kleemann, S. Kamba, T. Katsufuji, Large off-diagonal magnetoelectric coupling in the quantum paraelectric antiferromagnet $EuTiO_3$. *Phys. Rev. B* **81**, 064426 (2010).
63. C. J. Fennie, K. M. Rabe, Ferroelectric transition in $YMnO_3$ from first principles. *Phys. Rev. B* **72**, 100103 (2005).
64. J. Varignon, S. Petit, A. Gellé, M. B. Lepetit, An *ab initio* study of magneto-electric coupling of $YMnO_3$. *J. Phys. Condens. Matter* **25**, 496004 (2013).
65. J. Varignon, N. C. Bristowe, E. Bousquet, P. Ghosez, Magneto-electric multiferroics: Designing new materials from first-principles calculations. *Phys. Sci. Rev.* **5**, 20190069 (2020).
66. H. Schaal, J. Nuss, W. Hönle, Y. Grin, H. G. von Schnering, Crystal structure of tetraeuropium diantimonide oxide, Eu_4Sb_2O. *Z. Kristallogr.* **213**, 15 (1998).
67. N. A. Spaldin, M. Fiebig, The renaissance of magnetoelectric multiferroics. *Science* **309**, 391–392 (2005).
68. W. D. Brixel, J.-P. Rivera, A. Steiner, H. Schmid, Magnetic field induced magnetoelectric effects, $(ME)_H$, in the perovskites Pb_2CoWO_6 and Pb_2FeTaO_6. *Ferroelectrics* **79**, 201–204 (1988).
69. H. J. Zhao *et al.*, Near room-temperature multiferroic materials with tunable ferromagnetic and electrical properties. *Nat. Commun.* **5**, 4021 (2014).
70. W. Chen, J. George, J. B. Varley, G.-M. Rignanese, G. Hautier, High-throughput computational discovery of $In_2Mn_2O_7$ as a high Curie temperature ferromagnetic semiconductor for spintronics. *NPJ Comput. Mater.* **5**, 72 (2019).
71. S. V. Gallego, J. Etxebarria, L. Elcoro, E. S. Tasci, J. M. Perez-Mato, Automatic calculation of symmetry-adapted tensors in magnetic and non-magnetic materials: A new tool of the Bilbao crystallographic server. *Acta Crystallogr.* **A75**, 438–447 (2019).
72. Y. Wang, L. D. Calvert, E. J. Gabe, J. B. Taylor, Europium arsenic oxide Eu_4As_2O: A filled La_2Sb structure and its relation to the K_2NiF_4 and GeTeU types. *Acta Crystallogr.* **B33**, 3122–3125 (2010).
73. W. Hönle, H. Schaal, H. G. von Schnering, Crystal structure of tetraeuropium dibismuthide oxide, Eu_4Bi_2O. *Z. Kristallogr.* **213**, 16 (1998).
74. U. Burkhardt, M. Wied, W. Hönle, Yu. Grin, H. G. von Schnering, Crystal structure of tetraytterbium diarsenide oxide, Yb_4As_2O. *Z. Kristallogr. N. Cryst. Struct.* **213**, 13 (1998).
75. S. Klos, "Ternäre Zintl-Phasen (Erd)Alkalimetall-Triel-Pentel und deren partielle Oxidation zu Pentelidgallaten," PhD thesis, Rheinische Friedrich-Wilhelms-Universität Bonn, Bonn, Germany (2018).
76. J. Nuss, U. Wedig, M. Jansen, Geometric variations and electron localizations in intermetallics: The case of La_2Sb type compounds. *Z. Anorg. Allg. Chem.* **637**, 1975–1981 (2011).
77. A. Togo, I. Tanaka, Spglib: A software library for crystal symmetry search. arXiv [Preprint] (2018). https://arxiv.org/abs/1808.01590. Accessed 18 December 2020.
78. X. Gonze *et al.*, The ABINIT project: Impact, environment and recent developments. *Comput. Phys. Commun.* **248**, 107042 (2020).
79. G. Kresse, J. Hafner, Efficiency of ab-initio total energy calculations for metals and semiconductors using a plane-wave basis set. *J. Phys. Condens. Matter* **6**, 15 (1996).
80. G. Kresse, J. Furthmüller, Efficient iterative schemes for *ab initio* total-energy calculation using a plane-wave basis set. *Phys. Rev. B* **54**, 11169 (1996).
81. D. R. Hamann, Optimized norm-conserving Vanderbilt pseudopotentials. *Phys. Rev. B* **88**, 085117 (2013).
82. M. J. van Setten *et al.*, The PseudoDojo: Training and grading a 85 element optimized norm-conserving pseudopotential table. *Comput. Phys. Commun.* **226**, 39–54 (2018).
83. X. Gonze, First-principles responses of solids to atomic displacements and homogeneous electric fields: Implementation of a conjugate-gradient algorithm. *Phys. Rev. B* **55**, 10337–10354 (1997).
84. X. Gonze, C. Lee, Dynamical matrices, Born effective charges, dielectric permittivity tensors, and interatomic force constants from density-functional perturbation theory. *Phys. Rev. B* **55**, 10355–10368 (1997).
85. G. Kresse, D. Joubert, From ultrasoft pseudopotentials to the projector augmented-wave method. *Phys. Rev. B* **59**, 1758–1775 (1999).
86. J. George, Data from "Lobster calculations." Zenodo. doi.org/10.5281/zenodo.4529196. Accessed 1 March 2021.
87. M. Pajda, J. Kudrnovský, I. Turek, V. Drchal, P. Bruno, Ab initio calculations of exchange interactions, spin-wave stiffness constants, and Curie temperatures of Fe, Co, and Ni. *Phys. Rev. B* **64**, 174402 (2001).
88. E. Bousquet, N. A. Spaldin, K. T. Delaney, Unexpectedly large electronic contribution to linear magnetoelectricity. *Phys. Rev. Lett.* **106**, 107202 (2011).
89. J. Iniguez, First-principles approach to lattice-mediated magnetoelectric effects. *Phys. Rev. Lett.* **101**, 117201 (2008).

Downloaded at UNIVERSITE CATHOLIQUE DE LOUVAIN UCL on April 24, 2021